Numerical study into the morphology and formation mechanisms of three-dimensional particle structures in vibrated cylindrical cavities with various heating conditions

Marcello Lappa*
Department of Mechanical and Aerospace Engineering, University of Strathclyde, 75 Montrose Street, Glasgow G1 1XJ, United Kingdom
(Received 10 May 2016; published 17 October 2016)

The present analysis extends the author's earlier work [Lappa, Phys. Fluids **26**, 093301 (2014)] on the properties of patterns formed by the spontaneous accumulation and ordering of solid particles in certain types of flow. It is shown that under certain conditions, when subjected to vibrations to induce natural flow, nonisothermal fluids with dispersed solid particles are characterized by intervals of solid-pattern-forming behavior due to particle rearrangements preceded by intervals in which no recognizable structures of solid matter can be detected. The dynamics of these systems are highly nonlinear in nature. Because this family of particle attractors is known to exhibit strong sensitivity to the symmetry properties of the considered vibrated system and related geometrical constraints, the present study attempts to clarify the related dynamics in a geometry with curved walls (cylindrical enclosure). In particular, by assuming vibrations always directed perpendicularly to the imposed temperature gradient, we show that the morphology, spatial extension (percentage of physical volume occupied), separation (spatial distance), and mechanisms responsible for the formation of the resulting particle structures change significantly according to whether the temperature gradient is parallel or perpendicular to the symmetry axis of the cylinder. This indicates that the physics is not invariant with respect to 90° rotations in space of the specific forcing considered (direction of the imposed temperature gradient and associated perpendicular vibrations). Additional insights into the problem are obtained by assessing separately the influence played by the time-averaged (mean) and oscillatory effects. According to the numerical results, the intriguing diversity of particle agglomerates results from the different role or importance played by (curved or straight) boundaries in constraining particles and from the different structure and topology of the resulting macroscopic (large-scale) thermovibrational flow oscillating in time at the same frequency of the imposed vibrations.

DOI: 10.1103/PhysRevFluids.1.064203

I. INTRODUCTION

Fluids with dispersed solid particles have been widely used in industry. These applications span such diverse fields as cooling systems for nuclear reactors, heat exchangers, solar energy collectors, electronic industry, and a variety of modern processes for the production of new materials with improved physical and chemical properties (e.g., structural materials for marine and aerospace engineering, many types of composites, electrical conductors, and magnetic substances). Notably, the properties of these products are linked to their microscopic structure (their electrical and/or mechanical properties can be ascribed to characteristics such as high disorder, caging, and/or particle clustering on multiple length scales), which makes the study of the solid-liquid pattern formation a topic of great interest to materials engineers (see, e.g., Ref. [1]).

*marcello.lappa@strath.ac.uk; marlappa@unina.it

In spite of their great potentials, however, these special fluids are still in an early stage of exploitation. Indeed, from a theoretical viewpoint, such solid-liquid mixtures still represent a rather complex problem because it appears very difficult, if not practically impossible, to formulate any theory that can predict *a priori* their behavior. Among the phenomena to be taken into account for a possible prediction of the final distribution of particles in the liquid matrix, one should mention sedimentation (in the earth's gravitational field the usual differences in density cause rapid spatial separation of the solid phase through sedimentation or flotation), the presence of other body forces (e.g., electric and/or magnetic fields), and inertial clustering (the process of spontaneous grain aggregation determined by particle specific inertia and viscous drag in the presence of fluid convection).

In the present work, given the recent resurgence of theoretical studies exploring the consequences of particle clustering mechanisms [2–11] and in view of the generality of these structure-forming processes, we expressly concentrate on situations where particle inertia acts as the main pattern-forming driver. In particular, we consider particle aggregation and ordering mechanisms operating under the effect of alternating flows induced by vibrations (i.e., body accelerations varying sinusoidally in time). The specificity of the considered situation lies in the nature of the driving force, which has a zero-time-averaged value and which, accordingly, makes linear effects negligible; thereby only nonlinear effects are expected to be significant (even if they are small compared to the instantaneous linear effects). The reason for such a choice also resides in the fact that, like magnetic fields, vibrations allow contactless control of the flow and dispersed particles, but, unlike magnetic fields, they may be regarded as a new technique that can be used more universally, because its application is not limited to electrically conductive melts and particles.

Since the author's earlier analysis [12] was entirely concentrated on a geometrical configuration with straight walls (a cubical cavity) and a fixed direction of the temperature gradient, here we allow the problem to span two additional degrees of freedom, namely, the presence of curved sidewalls (cylindrical enclosure) and the relative direction of the imposed temperature gradient and vibrations with respect to such sidewalls. Natural convection induced by steady (terrestrial) gravity in fluid-filled cylinders has received enormous attention over the past several years due to its wide applications in engineering and technology [13–22]. For similar studies considering convective effects induced by time-varying accelerations rather than steady gravity, the reader may consider [23–31].

For what concerns the dynamics of solid particles transported by natural flows in such cylindrical configurations, available efforts seem to be very rare and sparse. Most analyses have concentrated on the case of particle clustering supported by Marangoni convection (see [32] and references therein; see also [33,34]) or Rayleigh-Bénard flow [35], which, however, pertains to a different category of phenomena. As outlined above, in this analysis, neither a steady external force field nor surface-tension-driven effects are considered; rather the dynamics are entirely produced by the interplay between an acceleration field varying sinusoidally in time, the resulting thermovibrational flow, and the response of particles (depending on their specific mass and size).

II. MATHEMATICAL FORMULATION

A. Vibrations

Perturbations induced in a fluid by a sinusoidal displacement of a fluid system along a given direction ($\hat{\mathbf{n}}$ is the related unit vector) $\mathbf{s}(t) = b\sin(\omega t)\hat{\mathbf{n}}$, where b is the amplitude and $\omega = 2\pi f$ (f is the frequency), induce an acceleration $\mathbf{g}(t) = g_\omega \sin(\omega t)\hat{\mathbf{n}}$, where $g_\omega = b\omega^2$ [36]. Such inertial perturbations are known to affect inhomogeneities present in the considered fluid system (see, e.g., [37]). These inhomogeneities may be due, on the one hand, to density variations induced in the fluid by temperature gradients (which lead to the so-called thermovibrational flow [38–40]) and, on the other hand (see, e.g., [41]) to the granular structure of the considered two-phase system (an assembly

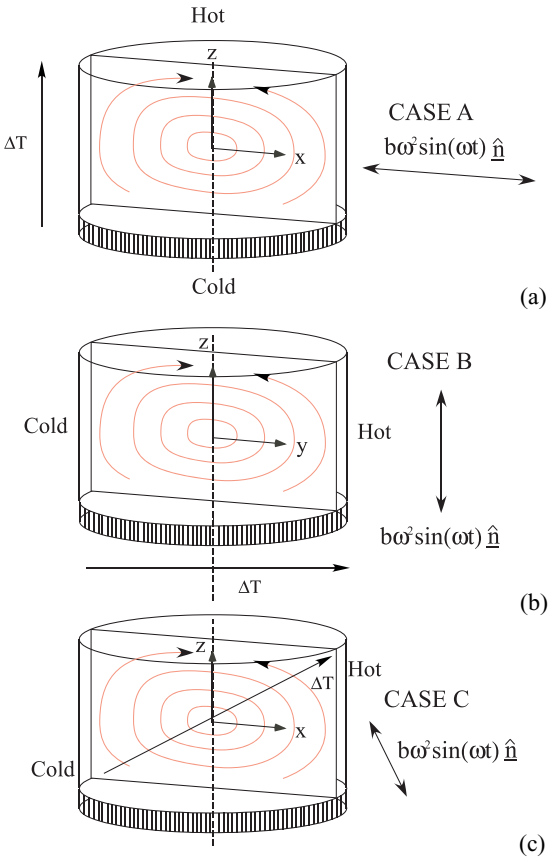

FIG. 1. Sketch of the configuration under investigation: (a) cylinder with differentially heated ends and adiabatic sidewall subjected to vibrations perpendicular to its axis, (b) cylinder with insulated ends and nonisothermal sidewall (temperature varying as a sinusoidal function of the azimuthal angle) subjected to vibrations parallel to its axis, and (c) cylinder with temperature varying on the boundary along both the axial and azimuthal directions and vibrations perpendicular to the imposed temperature gradient.

of hard spheres dispersed in the liquid in the present case). The related principles and governing equations will be illustrated in Secs. II C and II D, respectively.

B. System

Insights are sought from consideration of an archetypal setting corresponding to a differentially heated cylindrical cavity. In particular, a cylindrical enclosure with a height to diameter ratio $A = L/D = 0.75$ filled with $NaNO_3$ (sodium nitrate with $Pr = 8$) is examined. Following earlier computational studies reported in this area for the case of steady gravity (see the Introduction for existing studies in the literature), three main configurations are defined in the present work for what concerns thermal boundary conditions: (a) a differentially heated cylindrical enclosure with adiabatic conditions on the lateral wall, (b) a cylindrical enclosure limited axially by insulated solid walls with a temperature on the lateral wall varying as a sinusoidal function of the azimuthal angle, and (c) an intermediate configuration with temperature varying along both the axial and the azimuthal directions (Fig. 1). As the flow of thermovibrational nature induced by vibrations is known to be very sensitive to the relative angle between the imposed temperature gradient and the direction of vibrations [42], with the emerging convection being very weak or absent when such directions

are parallel (degenerate situation), here, in particular, without loss of generality, we concentrate expressly on the case of imposed periodic accelerations perpendicular to the imposed temperature difference ΔT (Fig. 1).

C. Nondimensional balance equations

Variables are nondimensionalized using conventional scalings: the coordinates by the axial system extension L and the velocity $\mathbf{V}$ by the energy diffusion velocity $V_\alpha = \alpha/L$, where α is the fluid thermal diffusivity, and time t and pressure p by, respectively, L^2/α and $\rho\alpha^2/L^2$, where ρ is the fluid density. Moreover, the temperature is measured with respect to its initial average value $\bar{T}_m$ and is made nondimensional as $T = (\bar{T} - \bar{T}_m)/\Delta T$.

In such a framework and using the Boussinesq approximation to account for the presence of body accelerations as defined in Sec. II A, the continuity and momentum equations simply read

$$\nabla \cdot \mathbf{V} = 0, \tag{1}$$

$$\frac{\partial \mathbf{V}}{\partial t} = -\nabla p - \nabla \cdot [\mathbf{V}\mathbf{V}] + \mathrm{Pr}\,\nabla^2 \mathbf{V} + \mathrm{Pr}\,\frac{b\omega^2 \beta_T \Delta T L^3}{\nu\alpha} T \sin\left(\frac{L^2\omega}{\alpha} t\right)\hat{\mathbf{n}}, \tag{2}$$

where $\frac{b\omega^2\beta_T \Delta T L^3}{\nu\alpha} = \mathrm{Ra}_\omega$ can be regarded as a variant of the classical Rayleigh number with the steady acceleration being replaced by the amplitude of the considered periodic acceleration (β_T is the thermal expansion coefficient). The problem, therefore, is reduced to four independent nondimensional parameters only, where the first is the well-known Prandtl number ($\mathrm{Pr} = \nu/\alpha$, where ν is the fluid kinematic viscosity) and the others are the nondimensional frequency ϖ, the nondimensional acceleration amplitude γ, and buoyancy factor β defined as

$$\varpi = \frac{\omega L^2}{\alpha}, \tag{3a}$$

$$\gamma = \frac{b\omega^2 L^3}{\alpha^2}, \tag{3b}$$

$$\beta = (\beta_T \Delta T). \tag{3c}$$

Accordingly, the momentum equation can be recast in condensed form as

$$\frac{\partial \mathbf{V}}{\partial t} = -\nabla p - \nabla \cdot [\mathbf{V}\mathbf{V}] + \mathrm{Pr}\,\nabla^2 \mathbf{V} + \gamma\beta T \sin(\varpi t)\hat{\mathbf{n}}, \tag{4}$$

where obviously $\mathrm{Ra}_\omega = \gamma\beta/\mathrm{Pr}$.

This equation must be supplemented with the energy balance equation, which with the considered reference units in nondimensional form reads

$$\frac{\partial T}{\partial t} + \nabla \cdot [\mathbf{V}T] = \nabla^2 T. \tag{5}$$

For $t = 0$, initial conditions corresponding to liquid at rest and thermally diffusive conditions are assumed. For $t > 0$, the boundary conditions at the solid walls simply reflect the well-known no-slip and impermeability properties of solid boundaries ($\mathbf{V} = \mathbf{0}$). We do not report them here explicitly for the sake of brevity (and given their extreme simplicity). For problem closure, such conditions, however, have to be supplemented with those for the energy equation, which change according to the specific configuration shown in Figs. 1(a)–1(c). In the first case, the top and bottom ($z = \pm 0.5$) walls of the domain are assumed here to be at uniform and constant (nondimensional) temperatures

$$T_0 = 1/2 \quad \text{at} \quad z = -0.5, \tag{6a}$$

$$T_1 = -1/2 \quad \text{at} \quad z = 0.5, \tag{6b}$$

while the lateral boundary is adiabatic, i.e.,

$$\partial T/\partial r = 0 \quad \text{at} \quad r = 1/2A, \quad 0 \leqslant \varphi \leqslant 2\pi, \quad -0.5 < z < 0.5. \tag{6c}$$

For the second configuration, such conditions have to be replaced by

$$\partial T/\partial z = 0 \quad \text{at} \quad z = \pm 0.5, \tag{7a}$$

$$T = (1/2)\sin(\varphi) \quad \text{at} \quad r = 1/2A, \quad 0 \leqslant \varphi \leqslant 2\pi, \quad -0.5 < z < 0.5. \tag{7b}$$

For the third case, they read

$$T = -(1/2)[(1/2)\sin(\varphi) + z] \quad \text{at} \quad r = 1/2A, \quad 0 \leqslant \varphi \leqslant 2\pi, \quad -0.5 \leqslant z \leqslant 0.5 \tag{8a}$$

$$T = -(1/2)[(1/2)\sin(\varphi) + z] \quad \text{at} \quad 0 \leqslant r \leqslant 1/2A, \quad 0 \leqslant \varphi \leqslant 2\pi, \quad z = \pm 0.5. \tag{8b}$$

D. Dispersed phase

The dynamics of particles are treated using the Lagrangian approach originally introduced by Maxey and Riley [43]). Such an approach relies on the assumption that the particle velocity can be decomposed into two different contributions, i.e., $\mathbf{V}_{\text{part}}(r,t) = \mathbf{V}(r,t) + v_1(r,t)$, where $\mathbf{V}$ is the velocity of the undisturbed flow at the same spatial position occupied by the considered particle (which would result if the boundary conditions at the particle surface were not applied) and v_1 is a perturbative component created by the fluid-particle interaction.

From physical arguments, it is known that the fluid force on the particle depends on the local fluid inertia (proportional to the local material derivative of $\mathbf{V}$) and also on the local stress created by the presence of the particle. In particular, the relaxational part of the particle inertia is strictly related to its mass resistance (preventing it from following instantaneously the velocity of the surrounding fluid), whereas the fluid drag tends to damp the particle velocity towards the local fluid velocity (within an inertial time τ that scales with the particle radius $\tilde{R}$ as $\tau = 2\tilde{R}^2/9\nu$) [44].

These effects can be properly modeled by considering relevant viscous and inertial terms in the Lagrangian equations used to track the evolution of the particle in space and time. Despite this obvious way of thinking, however, some additional simplifying assumptions have to be invoked. These additional conditions concern the reciprocal influence of particle motion on the large-scale flow and the particle-particle interplay [44–46]. Following a common practice in the related literature [32], here the so-called dilute particle model is used, i.e., it is assumed that while particles are transported by the large-scale flow, the influence they exert on such a flow and among them is negligible, in other words, the perturbative flow v_1 has a negligible effect on the unperturbed field (in the presence of vibrations, as shown by several authors, this assumption is reliable if the concentration of the dispersed phase in the flow is small, i.e., if the distance of a particle from others is much larger than their diameter; see, e.g. [2,47,48]; the interested reader is referred, in particular, to Fig. 4 in Ref. [2]).

Within such a framework, the resulting particle transport equation reads

$$\frac{du_{\text{part}}}{dt} = \frac{1}{\xi + 1/2}\left[-\frac{\text{Pr}}{\text{St}}(u_{\text{part}} - u) + \frac{3}{2}\frac{\partial u}{\partial t} + \frac{3}{2}(\mathbf{V}\cdot\nabla\mathbf{V})_u\right] + \frac{\xi - 1}{\xi + 1/2}\gamma\sin(\varpi t)\sin(\phi), \tag{9a}$$

$$\frac{dv_{\text{part}}}{dt} = \frac{1}{\xi + 1/2}\left[-\frac{\text{Pr}}{\text{St}}(v_{\text{part}} - v) + \frac{3}{2}\frac{\partial v}{\partial t} + \frac{3}{2}(\mathbf{V}\cdot\nabla\mathbf{V})_v\right] + \frac{\xi - 1}{\xi + 1/2}\gamma\sin(\varpi t)\cos(\varphi)\cos(\phi), \tag{9b}$$

$$\frac{dw_{\text{part}}}{dt} = \frac{1}{\xi + 1/2}\left[-\frac{\text{Pr}}{\text{St}}(w_{\text{part}} - w) + \frac{3}{2}\frac{\partial w}{\partial t} + \frac{3}{2}(\mathbf{V}\cdot\nabla\mathbf{V})_w\right] + \frac{\xi - 1}{\xi + 1/2}\gamma\sin(\varpi t)\sin(\varphi)\cos(\phi), \tag{9c}$$

where ϕ is the angle between the direction of the imposed vibrations and the xy plane, ξ is the ratio of the particle to the fluid density, and $(u_{\text{part}}, v_{\text{part}}, w_{\text{part}})$ and (u, v, w) are the particle and fluid (axial,

TABLE I. Liquid-solid system properties.

Fluid ($NaNO_3$) density ρ (kg m^{-3})	Kinematic viscosity ν (m^2 s^{-1})	Thermal diffusivity α (m^2 s^{-1})	Thermal expansion coefficient β_T(K^{-1})	Particle to liquid density ratio ξ
1904	1.27×10^{-6}	1.58×10^{-7}	1.25×10^{-3}	1.85

radial, and azimuthal) velocity components, respectively. Moreover,

$$(\mathbf{V}\cdot\nabla\mathbf{V})_u = \left(u\frac{\partial u}{\partial z} + v\frac{\partial u}{\partial r} + \frac{w}{r}\frac{\partial u}{\partial \varphi}\right), \tag{10a}$$

$$(\mathbf{V}\cdot\nabla\mathbf{V})_v = \left(u\frac{\partial v}{\partial z} + v\frac{\partial v}{\partial r} + \frac{w}{r}\frac{\partial v}{\partial \varphi} - \frac{w^2}{r}\right), \tag{10b}$$

$$(\mathbf{V}\cdot\nabla\mathbf{V})_w = \left(u\frac{\partial w}{\partial z} + v\frac{\partial w}{\partial r} + \frac{vw}{r} + \frac{w}{r}\frac{\partial w}{\partial \varphi}\right). \tag{10c}$$

As discussed, e.g., in Ref. [41], the underlying assumptions on which this approach is based are a perfectly spherical shape of the solid particles and a very small value ($\ll$1) of the particle to fluid system characteristic size ratio $\tilde{R}/L$. This implies that $\mathrm{St} = \tau\nu/L^2 \ll 1$, where τ is the aforementioned particle relaxation time and St is the well-known Stokes number. Although Eq. (9) properly accounts for the motion of solid particles in the liquid phase, it is clear, however, that particles moving close to the solid boundaries require a special treatment (given the no-slip properties of such surfaces acting as sinks of momentum and therefore as a potential particle-entrapping loci). Following earlier studies, in particular, we assume particles to interact in a nonelastic fashion with walls [32,33].

E. Numerical method and code validation for buoyancy flow

Balance equations (1)–(5) have been solved numerically by a time-explicit finite-difference method (primitive-variable method) based on a cylindrical mesh and a staggered collocation of fluid-dynamic variables. Forward differences in time and central-differencing schemes in space (second-order accurate) have been used to discretize the energy and momentum governing equations. The related solution strategy is not discussed here; the interested reader is referred to various books in the literature for an exhaustive treatment, e.g. [49] (here we just limit ourselves to recalling that such an approach is based on the well-known pressure-velocity coupling strategy based on the application of the momentum equation to derive an equation for pressure via the time-discretized continuity equation). For the specific case of convection induced by buoyancy, the present code was validated through comparison with the classical three-dimensional solutions reported by Bontoux *et al.* [16] (see Fig. 2).

F. Case of interest

The properties of the considered solid-liquid system are summarized in Table I. Assuming an axial extension of the cylindrical enclosure $L = 2 \times 10^{-2}$m, the following values of characteristic nondimensional parameters are considered: $\varpi = 10^3$ and $\gamma = 1.5 \times 10^6$, which correspond to $\mathrm{Ra}_\omega = 1.58 \times 10^4$. This is also equivalent to considering a value of the so-called Gershuni number

$$\mathrm{Gs} = \frac{(b\omega\beta_T\Delta T L)^2}{2\nu\alpha} = \frac{(\beta_T\Delta T L)^2}{2\nu\alpha}\left(\frac{g_\omega}{\omega}\right)^2 = \frac{\varpi^2\Lambda^2}{2\,\mathrm{Pr}} = \frac{1}{2\,\mathrm{Pr}}\left(\frac{\beta\gamma}{\varpi}\right)^2 = 10^3. \tag{11}$$

Such a parameter (which, in general, accounts for the intensity of time-averaged convection resulting from the application of high-frequency vibrations; see, e.g., [42]) is fixed to $\mathrm{Gs} = 10^3$ so as

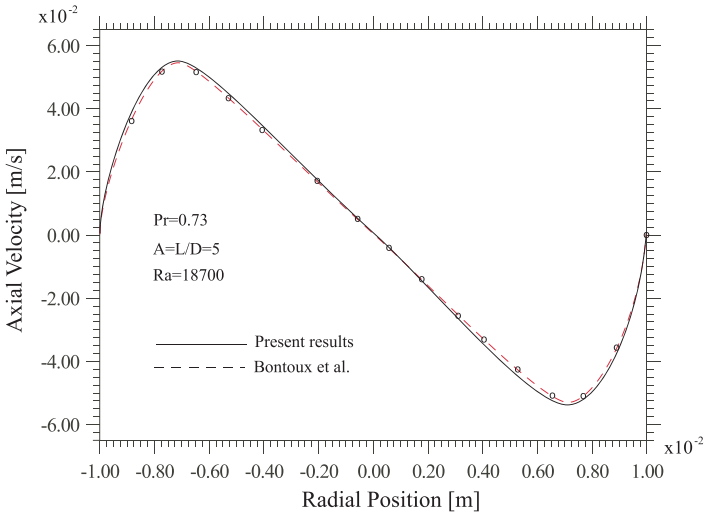

FIG. 2. Comparison with the results reported by Bontoux *et al.* [16]: differentially heated horizontal cylinder with $\mathrm{L} = 10^{-1}\mathrm{m}, A = 5, \mathrm{Pr} = 0.73$, and $\mathrm{Ra} = 1.87 \times 10^4$ ($N_z \times N_r \times N_\varphi$ mesh $65 \times 16 \times 32$).

to guarantee that time-averaged convective effects of thermovibrational nature are very small with respect to the oscillatory component of fluid velocity. This also guarantees a negligible departure of the time-averaged temperature field from the purely diffusive conditions (i.e., the distribution of temperature inside the enclosure can be assumed to be almost linear).

The density of the particles is also considered fixed: $\xi = 1.85$, such a value corresponding to typical tracers used in experiments with $NaNO_3$ [4]. Their characteristic size gives $\eta = (\xi - 1)\mathrm{St}/\mathrm{Pr} = 10^{-4}$, this value of η being a good compromise between two opposite needs (as further explained in the following). As shown by Lappa [12] (to which the reader is referred for an exhaustive treatment of such aspects), the formation of recognizable particle structures in the presence of thermovibrational flow takes a time that decreases as the particle size is increased; particle accumulation, however, is found not to occur when the particle size exceeds a given threshold. Accordingly, the specific value $\eta = 10^{-4}$ has been selected in the present work with the twofold purpose to shorten the otherwise computationally prohibitive time required for the formation of well-defined particle patterns on the one hand and not to exceed the above-mentioned limit in terms of particle size (beyond which such patterns are no longer formed) on the other hand.

G. Grid refinement study and code validation for thermovibrational convection

The ability of the present code to correctly capture the particle dynamics in flows of oscillatory nature in cylindrical geometries was already assessed to a certain extent in earlier studies. As an example, this was verified for the case of a traveling wave in Ref. [33] (where the results provided by the present code were quantitatively compared with those by Melnikov *et al.* [4]) and in Ref. [34] for the case of a standing wave (where the present code was used to reproduce the dynamics presented by Schwabe and Mizev [10]). The limits of applicability of the considered multiphase approach in capturing particle dynamics induced by high-frequency vibrations were further assessed by [41] (all these studies considered the same value of the Prandtl number assumed here, namely, $\mathrm{Pr} = 8$).

As usual, in the present work, the convergence behavior of the code in terms of its ability to produce a mesh independent solution (in terms of both fluid velocity field and resulting particle structures) has been assessed via an *a priori* grid tailoring process. In particular, such an assessment has been conducted assuming as sensitive parameters (to check grid convergence) the maximum (asymptotic) value attained by each of the velocity components u, v, and w. Owing to the nature

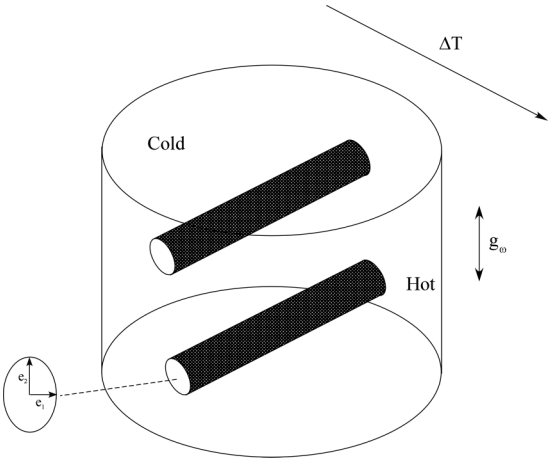

FIG. 3. Sketch of cylindrical enclosure, related thermal boundary conditions, imposed vibrations, and emerging particulate aggregates.

of the specific problem under investigation (able to produce a steady mean flow field as well as well-defined particle structures with time-independent properties), such a study has also taken into account time-averaged quantities and measurable characteristics of the emerging particulate structures. The time-averaged velocity components have been computed, respectively, as

$$\langle u\rangle = \frac{\varpi}{2\pi}\int_0^{2\pi/\varpi} u(t)dt, \quad \langle v\rangle = \frac{\varpi}{2\pi}\int_0^{2\pi/\varpi} v(t)dt, \quad \langle w\rangle = \frac{\varpi}{2\pi}\int_0^{2\pi/\varpi} w(t)dt, \tag{12}$$

with $u(t)$, $v(t)$ and $w(t)$ being provided by the solution of the set of equations presented in Sec. II C.

For code validation purposes, these quantities (and related patterns in space) have been also determined resorting to an independent code based on the solution of the so-called Gershuni system of equation. These alternate sets of equations, based on the introduction of a potential flow variable, can be used to determine directly the time-averaged flow with no need to solve the complete set of Navier-Stokes equations (these equations, traditionally used in the literature for validation purposes in the case of flows with thermovibrational nature, are not described here, the reader being referred, e.g., to [38] for additional details). As a relevant and representative case for such an extensive assessment, in particular, we focused on the case corresponding to the conditions shown in Fig. 1(b), for which the emerging particle structures have a relatively simple shape that allows their typical size to be measured precisely [namely, the lengths e_1 and e_2, representing the axes of the elliptical cross section given by the intersection of the emerging particle structures with the center plane yz (see Fig. 3)].

The outcomes of such a parametric investigation are summarized in Table II. Table II(a) indicates that the grid independence of the flow of thermovibrational nature could be attained even with the coarsest mesh considered in the table (the values obtained with a grid $20 \times 14 \times 20$ match a reasonable approximation ($<1\%$) of the values obtained with finer grids). This result can be easily explained according to the nature of the emerging flow, which apart from being very slow is regular and smooth in time and space with no thermal or kinematic boundary layers.

The velocities shown in Table II would correspond in dimensional form for a cylinder with height 2×10^{-2} m to a maximum velocity $\cong 2 \times 10^{-4}$m/s and a maximum corresponding time-averaged velocity $\cong 2 \times 10^{-6}$ m/s (among other things this also confirms our initial assumption about the time-averaged convective effects of thermovibrational nature being very small with respect to the oscillatory component of fluid velocity, i.e., $\langle u\rangle_{\max}/u_{\max} \cong \langle v\rangle_{\max}/v_{\max} \cong \langle w\rangle_{\max}/w_{\max} \cong 10^{-2}$). Nevertheless, Table II(b) also clearly indicates that a finer mesh is required for attaining a reasonable

TABLE II. Grid refinement study: maximum of the velocity components of the **V** and $\langle \mathbf{V} \rangle$ and fields and size of axes e_1 and e_2 shown in Fig. 3 as a function of mesh resolution (cylindrical enclosure with differentially heated sidewall and adiabatic ends, vibrations along the z axis, $\mathrm{Pr} = 8, A = 0.75, \varpi = 1 \times 10^3, \mathrm{Ra}_\omega = 1.58 \times 10^4$, and $t = 0.56$).

(a)

$N_z \times N_r \times N_\varphi$	$u_{\max}$	$v_{\max}$	$w_{\max}$
$20 \times 14 \times 20$	22.090459	23.988021	22.126823
$27 \times 18 \times 27$	21.886765	23.898973	21.874763
$41 \times 27 \times 41$	21.825312	23.857689	21.842886
$49 \times 33 \times 49$	21.814679	23.835055	21.835362

(b)

Mesh	$\langle u \rangle_{\max}$	$\langle v \rangle_{\max}$	$\langle w \rangle_{\max}$	$e_1 \times 2$	$e_2 \times 2$
$20 \times 14 \times 20$	0.3027287	0.3739038	0.2536782	0.082	0.234
$27 \times 18 \times 27$	0.3023345	0.3685796	0.2423693	0.094	0.253
$41 \times 27 \times 41$	0.3021813	0.3552482	0.2318292	0.118	0.270
$49 \times 33 \times 49$	0.3020539	0.3531231	0.2296784	0.121	0.274

(c)

$41 \times 27 \times 41$	$\langle u \rangle_{\max}$	$\langle v \rangle_{\max}$	$\langle w \rangle_{\max}$
present code	0.3021813	0.3552482	0.2318292
Gershuni's framework	0.2987363	0.3489834	0.2268736

level of convergence in the typical size of the resulting particle structures (a mesh with at least $N_z \times N_r \times N_\varphi = 41 \times 27 \times 41$ points is required to make the percentage variation of e_1 and e_2 less than 3% with respect to the next row in the table). Additional validation for the present code has been provided by the very good agreement between the time-averaged quantities obtained in the framework of the so-called Gershuni approach discussed before [Table II(c)]. Figure 4 shows the time-averaged pattern in the yz plane, corresponding to the well-known quadrupolar field [39,50] that emerges in closed cavities for vibrations perpendicular to the temperature gradient.

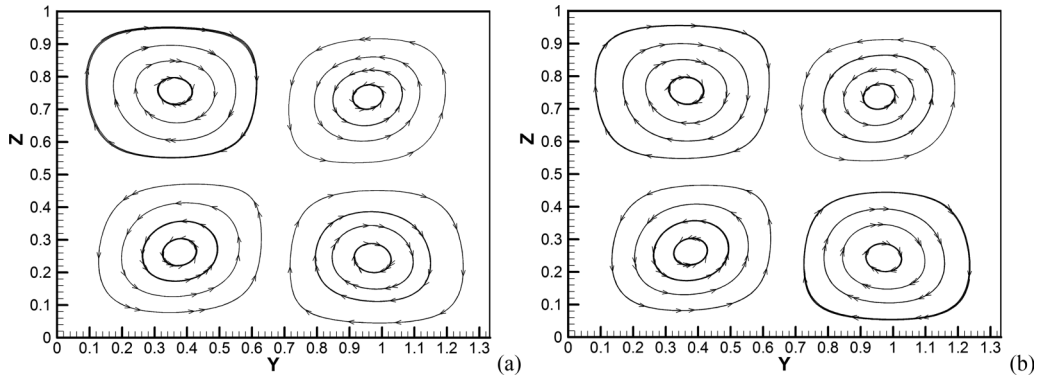

FIG. 4. Classical quadrupolar flow field in the yz plane obtained by (a) time averaging of the oscillatory solution and (b) integration of the Gershuni equations (cylinder with insulated ends and nonisothermal sidewall with temperature varying as a sinusoidal function of the azimuthal angle, vibrations along the z axis, $\mathrm{Pr} = 8, A = 0.75, \varpi = 1 \times 10^3$, and $\mathrm{Ra}_\omega = 1.58 \times 10^4$).

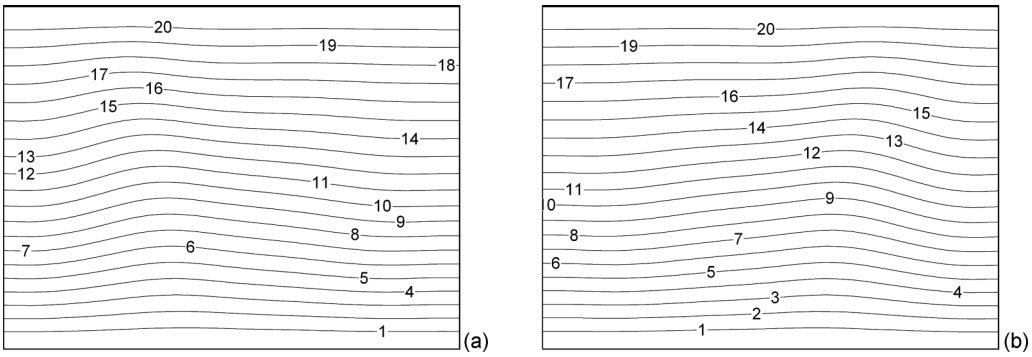

FIG. 5. Snapshots of the temperature distribution in the meridian plane xz ($\varphi = 0$) at two instants during the period τ of oscillation (case A) (contour legend: level $1 \rightarrow T = -0.45$, level $20 \rightarrow T = 0.45$, and $\Delta_{\text{level}} \rightarrow 0.05$): (a) $t = t_0$ and (b) $t = t_0 + \tau/2$ ($\tau = 2\pi/\varpi$).

III. RESULTS

The author's earlier analysis [12] was entirely concentrated on a geometrical configuration with straight walls (a cubical cavity) and a fixed direction of the temperature gradient, allowing most of the involved parameters (the amplitude and angular frequency of the acceleration disturbance, and the particle Stokes number) to span relatively wide ranges. As the focus here is on the influence of curved walls in producing specific behaviors, we keep constant most of those parameters ($\text{Pr} = 8, A = 0.75, \varpi = 1 \times 10^3, \text{Ra}_\omega = 1.58 \times 10^4, \gamma = 1.5 \times 10^6$, and $\eta = 1 \times 10^{-4}$) while allowing the specific forcing considered (direction of the imposed temperature gradient and associated perpendicular vibrations) to have different orientations in space (as shown in Fig. 1). To track the system evolution, solid particles ($\cong 4 \times 10^4$) are initially seeded uniformly into the computational domain assuming their velocity equal to zero (to reflect the quiescent conditions of the surrounding liquid).

A. Differentially heated ends and adiabatic sidewall

1. Thermofluid-dynamic field

Figures 5 and 6 show the spatiotemporal evolution of the velocity and temperature field during half of a cycle of forcing in the case of a temperature gradient parallel to the system symmetry axis, insulated sidewall, and vibrations aligned with the x axis (case A). It is worth starting the related

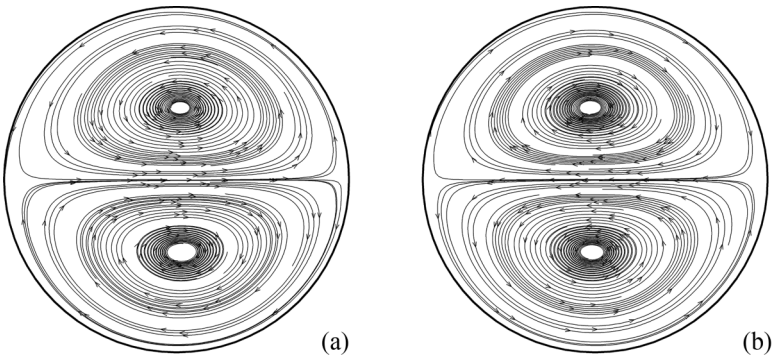

FIG. 6. Snapshots of the velocity field in the cross section $z = 0$ at two instants during the period τ of oscillation (case A): (a) $t = t_0$ and (b) $t = t_0 + t/2$ ($\tau = 2\pi/\varpi$).

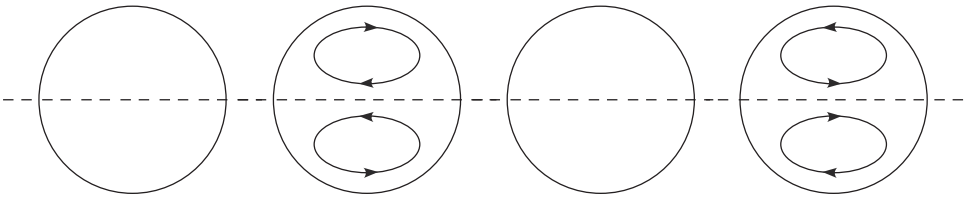

FIG. 7. Sequence (sketch) showing the evolution of vibration-induced convective cells in the generic cross section $z = \text{const}$ during one period of oscillation (case A).

discussion from the relatively simple observation that while, as expected (due to the relatively small value of the Gershuni number), the departure of the temperature field from purely diffusive conditions (a purely linear distribution of temperature along the z axis) is relatively weak (see Fig. 5), well-defined convective structures are visible at any instant in any cross section $z = \text{const}$ [e.g., $z = 0$ (see Fig. 6)].

In practice, regardless of the considered time, convective flow consists essentially of two main rolls with axis extended along the z direction, one being the mirror image of the other and having sense of circulation depending on the specific instant considered within the cycle of forcing. The intersection of such axial rolls with cross sections $z = \text{const}$ produces two apparent cells, one oriented clockwise and the other counterclockwise. These convective cells are not stationary and change their sense of rotation periodically [their intensity is not constant in time; if the considered convective cell is oriented clockwise during the first half-period of oscillation, then during the second half it vanishes and finally reappears in the same position oriented counterclockwise (see Fig. 7)]. Therefore, a clear distinguishing mark of this convective mode is the mental divisibility (topology) of the flow configuration in two semicircular regions (such a divisibility can be sketched, as shown in Fig. 8, by introducing an ideal plane of symmetry (PS) AB that separates the flow configuration into two sectors). At one end of the PS two opposite azimuthal currents originate and at the other end of the PS they vanish. Assuming that at a given instant $t = 0$ the starting point of such counterpropagating flows is the point A on the left side, two initially very close parcels of fluid located there at $\varphi = \pi^+$ and $\varphi = \pi^-$, respectively [see Fig. 8(a)] will move towards the right side (point B) as t increases, one in a clockwise direction [top semicircumference in Fig. 8(a)] and the other counterclockwise [bottom semicircumference in Fig. 8(a)]. In particular, both parcels will move with identical and constant velocity and after a duration of one-half of the vibration frequency ($t = 1/2f$) they reunite at the opposite side of point A (point B). At time $t = 1/f$, however, as the time-varying acceleration induced by vibrations changes sign, the same process will be repeated with two parcels initially located at $\varphi = 0^-$ and $\varphi = 0^+$, respectively, moving towards the left side in a clockwise direction along the bottom semicircumference and in the counterclockwise direction along the top semicircumference. As a natural consequence of such a mechanism, the instantaneous return

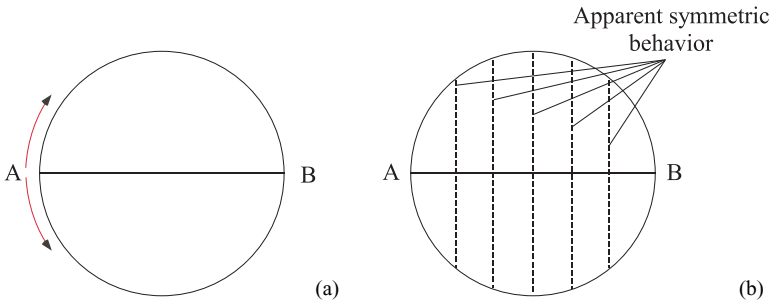

FIG. 8. Mental divisibility (topology) of the flow configuration (sketch).

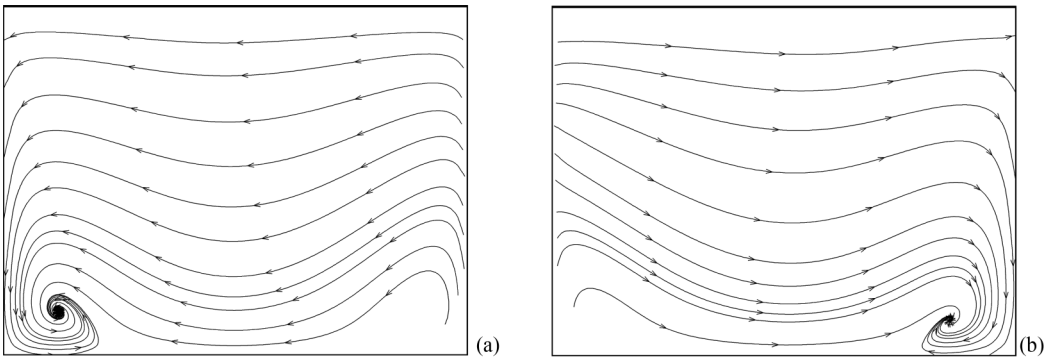

FIG. 9. Snapshots of velocity field in the meridian plane xz ($\varphi = 0$) at two instants during the period τ of oscillation (case A): (a) $t = t_0$ and (b) $t = t_0 + \tau/2$ ($\tau = 2\pi/\varpi$).

flow will tend to be aligned with the AB direction (i.e., with the direction of imposed vibrations) and the overall flow will display a mirror symmetry with respect to this direction in any section perpendicular to the PS [whereas it will appear strongly asymmetric in any section parallel to the x axis (Fig. 9)].

2. Particle structures

As shown in Fig. 10, after a relatively long transient time, well-defined particle structures are formed in the cylinder. Particles are no longer uniformly spaced in the liquid; rather they accumulate preferentially on spatially extended surfaces located in proximity to the lateral sidewall.

Most surprisingly, although such structures tend to retain the mirror symmetry with respect to the plane AB (the x axis, i.e., the direction of applied vibrations) and to reflect the typical topology of flow induced by vibrations (with fluid moving alternatively back and forth along the sidewall between points A and B), some regions completely depleted of particles appear periodically in the cylinder (clearly visible especially in the right part of Fig. 10). Such zones are separated from regions in which solid particles are more or less uniformly dispersed by the aforementioned spatially extended surfaces along which particles undergo preferential accumulation.

The subsequent evolution consists essentially of a rhythmic left-right displacement of the overall pattern and related characteristic independent loops visible in cross sections. This means that the system response to the imposed vibration is synchronous (or harmonic) (particles and velocity fields oscillating at the same frequency of the imposed sinusoidal forcing). In other words, once the particle-dense surfaces are formed, a further increase of time produces no variation in the morphological and topological properties of the pattern. Under the effect of vibrations, the pattern oscillates back and forth along the direction of vibrations essentially as a whole at the vibration frequency as experienced by an observer in the laboratory (fixed) reference frame [compare, e.g., Figs. 10(a) and 10(c); although the overall pattern is shifted to the right in Fig. 10(a) and to the left in Fig. 10(c), the characteristic size of the two circuits and their distance remain constant].

An interesting behavior, deserving some additional discussion, is evident along the line AB (see Fig. 10, right). A dark region (particle-dense spot) where particles accumulate is visible near the symmetry axis in the right part of Figs. 10(a) and 10(c) [no dark region is visible in Fig. 10(b)].

This process can be explained by resorting to an analogy with similar pluming phenomena in thermal convection. Just as in classical thermal-plume formation mechanisms, the heated fluid rises due to buoyancy along a vertical line, producing a cap on top as a result of the drag exerted on it by the overlying fluid (the result in the temperature map is something that looks like a mushroom); here the strong alternating flow along the line AB produces periodically a plume of particles moving

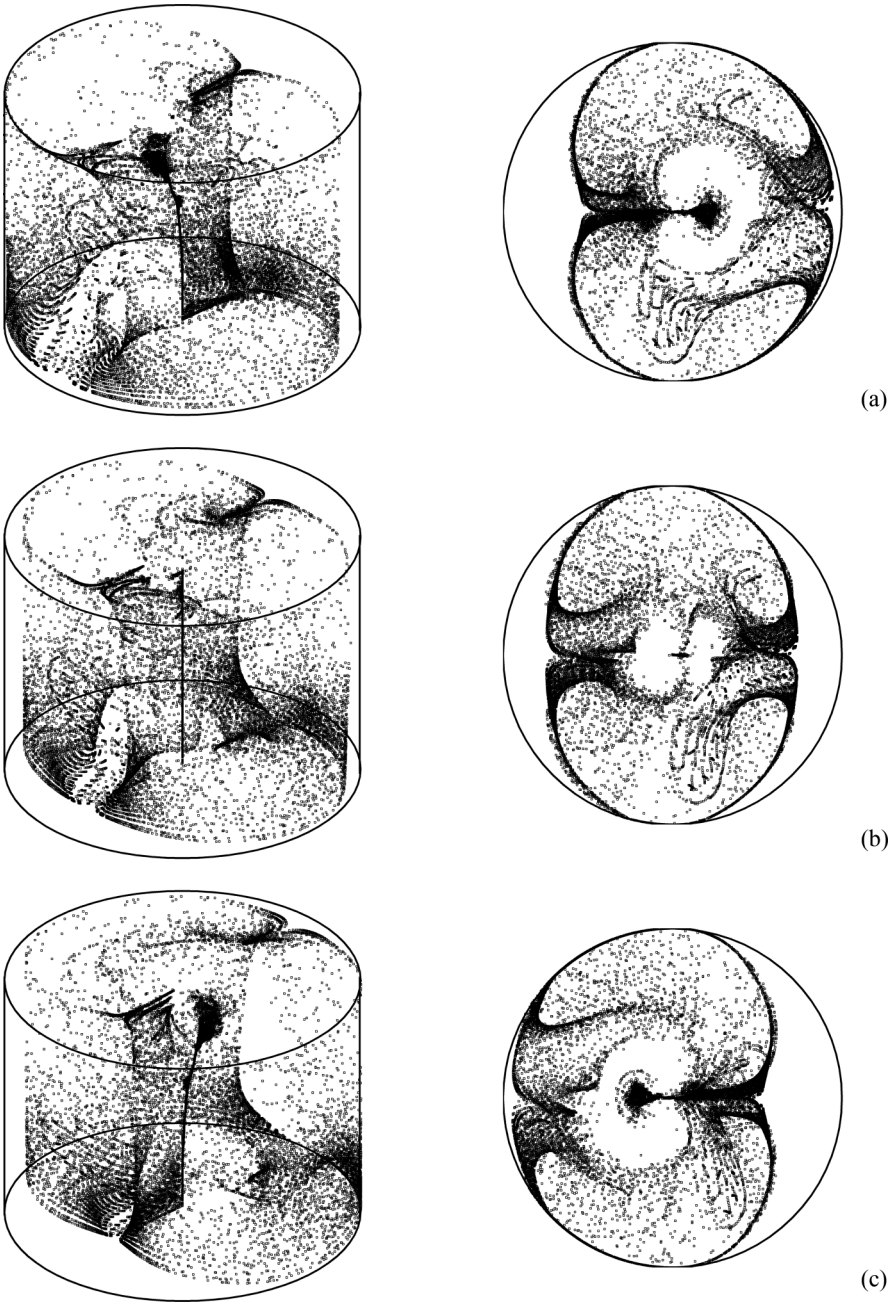

FIG. 10. Three-dimensional snapshots of particle aggregates (case A): (a) $t = t_0$, (b) $t = t_0 + \tau/4$, and (c) $t = t_0 + \tau/2$ ($t_0 = 1.4 \times 10^{-1}$ and $\tau = 2\pi/\varpi$).

from left to right or in the opposite direction. The concentration of particles in the plume cap is due essentially to the inertia that tends to slow down their motion with respect to the carrier liquid. In line with such an analogy, this plume effect disappears when the fluid velocity along AB is weakened [Fig. 10(b)].

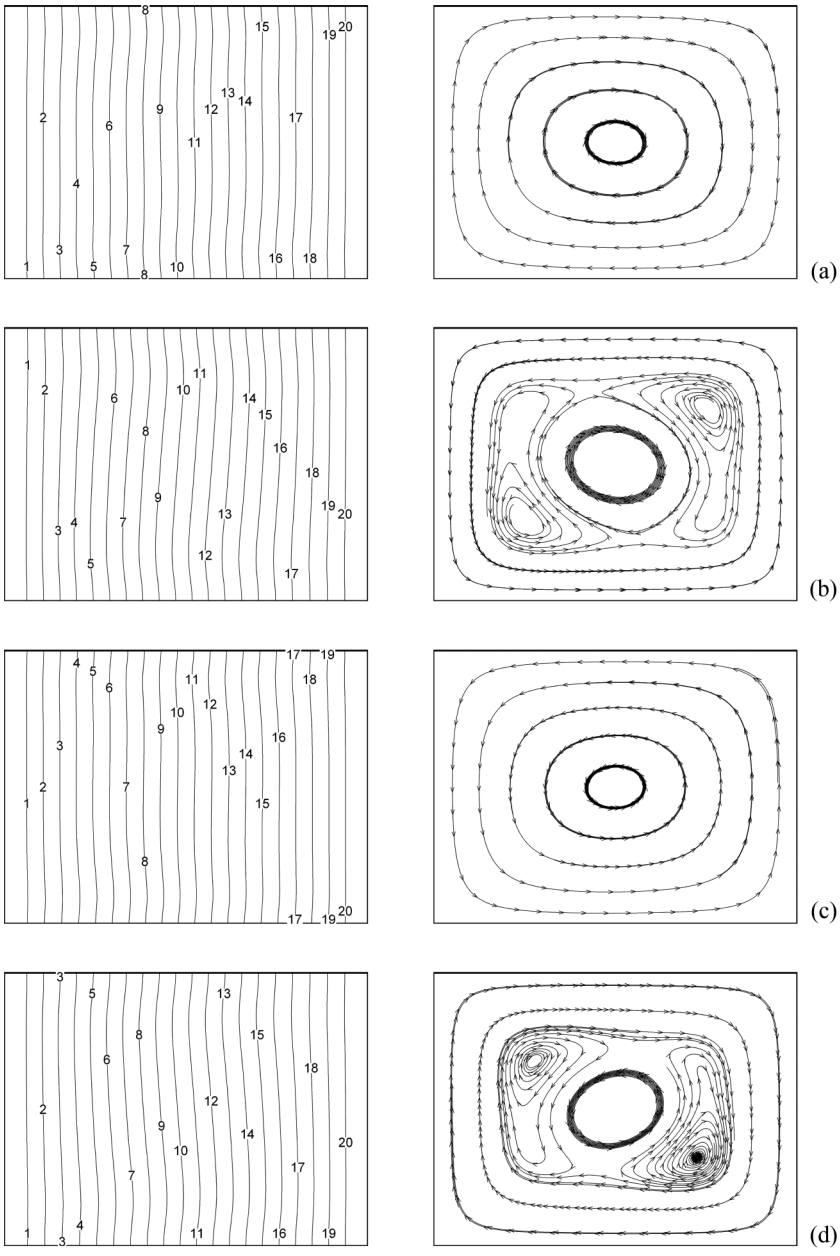

FIG. 11. Snapshots of temperature distribution (left) and velocity field (right) in the meridian plane yz ($\varphi = \pi/2$) at four instants evenly space in time during the period τ of oscillation (case B) (contour legend: level 1 $\rightarrow$ $T = -0.45$, level 20 $\rightarrow$ $T = 0.45$, and $\Delta_{\text{level}} \rightarrow 0.05$): (a) $t = t_0$, (b) $t = t_0 + \tau/4$, (c) $t = t_0 + \tau/2$, and (d) $t = t_0 + 3\tau/4$ ($t = 2\pi/\varpi$).

B. Nonisothermal sidewall and adiabatic bases

1. Thermofluid-dynamic field

Figure 11 shows that the flow structure changes completely when the adiabatic lateral boundary is replaced by a nonisothermal sidewall (with a resulting temperature gradient along the y direction

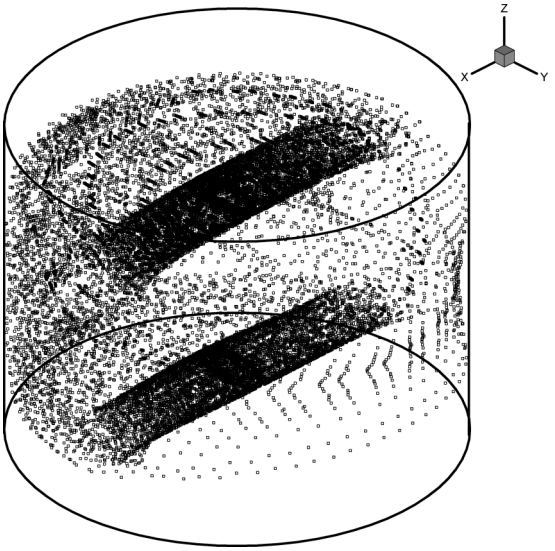

FIG. 12. Three-dimensional snapshots of particle aggregates (case B) ($t = 5.6 \times 10^{-1}$).

and perpendicular accelerations, i.e., vibrations aligned with the z axis). Given the relatively small value of the Gershuni number, the temperature distribution is still approximately linear inside the cylindrical enclosure (Fig. 11, left). The convective rolls with axis parallel to z, alternating their sense of rotation as time passes that we have seen in Sec. III A, however, are no longer a feature of the flow. Rather (Fig. 11, right, to be compared with Fig. 9) it displays a single main roll with axis parallel to x, changing cyclically its sense of rotation (from the clockwise sense to the counterclockwise one for increasing values of t). Such a main roll is produced essentially by the interplay between the temperature distribution and the buoyancy effect originating from the vibration-induced acceleration. More precisely, vibration-induced buoyancy and the imposed temperature gradient alternatively cooperate to produce a clockwise or counterclockwise convective cell over a cycle of the modulation. In that part of the cycle where the acceleration is directed along the positive x axis direction, the resulting convective cell is oriented counterclockwise and vice versa [clockwise-oriented roll when $g_\omega(t)$ changes its sign]. The concept of mental divisibility of the flow configuration in two mirror regions is still applicable, but, obviously, in this case the ideal plane of symmetry coincides with the xz plane.

2. Particle structures

As shown in Fig. 12, after a relatively long transient time, well-defined particle patterns are formed in the cylinder. Particles are no longer uniformly spaced in the liquid and, as in the case treated in Sec. III A, they tend to accumulate on spatially extended surfaces.

Most surprisingly, however, the volume percentage occupied by such surfaces is relatively small in comparison to the companion case discussed in Sec. III A. Two distinct tubular structures can be recognized in Fig. 12 that are very similar to those that would be obtained in the case of a cubical cavity [12]. Their overall radial extension is approximately equal to the diameter of the cylindrical enclosure and their orientation is parallel to the x axis. The two surfaces, however, are well separated (their axial distance is approximately 40% of the cylinder height). Both tubular structures have an elliptic-shaped section (obtained by intersection with the yz plane). The characteristic sizes of their elliptic section e_1 and e_2 are only 12% and 26% of the cylinder axial extension, which may be regarded as a clear distinguishing mark with respect to the situation considered in Sec. III A (obviously, another clear difference is given by the shape of the section *per se*, as the section shape of the tubular structures

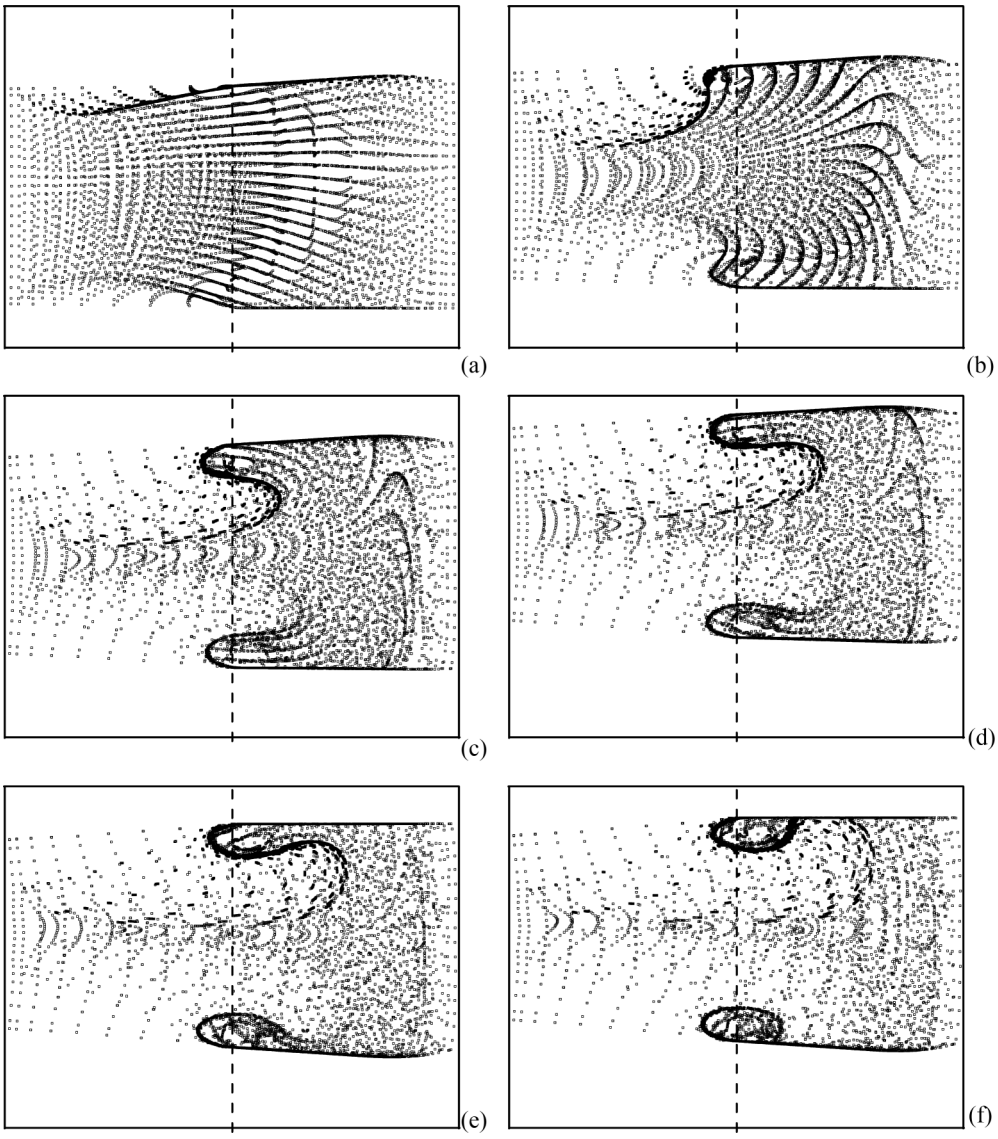

FIG. 13. Lateral view (from the x axis perspective) of particle aggregates as a function of time (case B): (a) $t = 2.7 \times 10^{-2}$, (b) $t = 9.5 \times 10^{-2}$, (c) $t = 1.6 \times 10^{-1}$, (d) $t = 1.9 \times 10^{-1}$, (e) $t = 2.24 \times 10^{-1}$, and (f) $t = 2.56 \times 10^{-1}$.

shown in Fig. 10, was more similar to an orange slice than to an ellipse). To fully understand the mechanism at work in this case (and appreciate the related theoretical implications), however, we have to examine in detail the spatiotemporal interplay established between buoyancy-induced flow and particle aggregates.

It is indeed the mechanism produced by the instantaneous (oscillating in time) flow (Fig. 11, right), in combination with vibration-induced particle time displacements whose nonlinear effects on particles accumulate over time, that leads to the observed particulate pattern. This is clearly illustrated in Fig. 13, which shows the stages of evolution of the considered system from the initial condition with particles uniformly distributed in the fluid up to the emergence of the final pattern with tubular structures aligned with the x axis.

At the beginning [Fig. 13(a)] particles close to the walls tend to be clustered owing to edge effects into two separate surfaces extended along the direction perpendicular to the imposed vibrations. In practice, this is due to the fact that when a group of particles moving under the effect of the vibration-induced periodic force (along z) comes in proximity to one of the two cylinder bases, they are accumulated along the boundary direction owing to the well-known impenetrability property of solid walls. This is reflected in the formation of an apparently marked (particle-dense) line in the lateral view shown in Fig. 13. When the periodic force changes its sign and particles move in the opposite direction, the above process results in the appearance of a particle-dense line separating the region containing particles from the pure liquid (particle-depleted region).

One must keep in mind, however, that, as illustrated in Sec. III B 1, the influence of vibrations is not limited to the periodic force exerted on particles along the z direction. They also produce flow of thermovibrational nature (Fig. 11) that can transport particles. This is essentially the reason why the above-mentioned particle-dense surfaces produced by the interaction with solid ends are stretched and folded as time passes.

The mechanism of pattern formation consists basically of a progressive translation away from the walls of particle dense lines and ensuing folding towards the interior of their part located in the cold region of the plane [Fig. 13(b)]. Such a folding is due essentially to the instantaneous motion of fluid shown in Fig. 11, which is alternatively accelerated from the hot side to the cold side (due to buoyancy) along the top or bottom wall (depending on the instantaneous direction of acceleration) and then released in the cold region of the cylindrical enclosure. This process is responsible for the formation in the initial stages of evolution of a horizontal amphoralike shape as seen in the yz plane (the distribution of particles results in a shape that bulges out above $y = 0$ and necks in below it).

As time increases, the progressive deformation of the lines delimiting the region with particles produces two rounded patches protruding from the main particle region towards the cold side. Figures 13(c) and 13(d) show that, as time increases, the extension of the two small areas hanging out from the main particle region becomes increasingly elongated (along the y direction) and contracts until a neck is formed for each of them [Fig. 13(e)]. As time is further increased, the size of such a neck shrinks spontaneously and finally the protuberant regions detach from the "mother" particle region [Fig. 13(f)] forming two independent loops (tubular structures). Therefore, the following main stages of evolution can be identified in the process leading to the formation of the pattern. In stage I the reason for the formation of a region where particles tend to concentrate is due to the interaction of particles with boundaries and the well-known impenetrability property of solid walls. In stage II the changes in the shape of the boundary separating the region with particles from the particle-depleted space are due to the convective particle transport produced by the instantaneous flow of thermovibrational nature; such changes lead to the formation of two elongated particle regions protruding in the particle-depleted space. Stage III begins when, owing to convective effects, the axial extension of the protuberant regions becomes very small at a certain location along y; for a further increase in time, the size of the neck decreases rapidly to zero, forming two well-defined tubular surfaces visible in Fig. 12 (whose intersection with the yz plane has approximately an elliptic shape).

The recognizable shapes formed by particles then stabilize in time. Indeed, the subsequent evolution consists essentially of a further depletion of the mother particle region with ensuing accumulation of particles in the two closed loops and a rhythmic (synchronous) top-bottom displacement of the overall pattern along the z direction. As in the companion case considered in Sec. III A, once the two particle circuits are formed, a further increase of time produces no variation in the morphological and topological properties of the pattern, which undergoes rhythmic displacement along the z direction as an apparently solid unit (although, at the risk of repetition, we should recall that the property of all particles of moving as they pertained to a solid lattice is just an illusion).

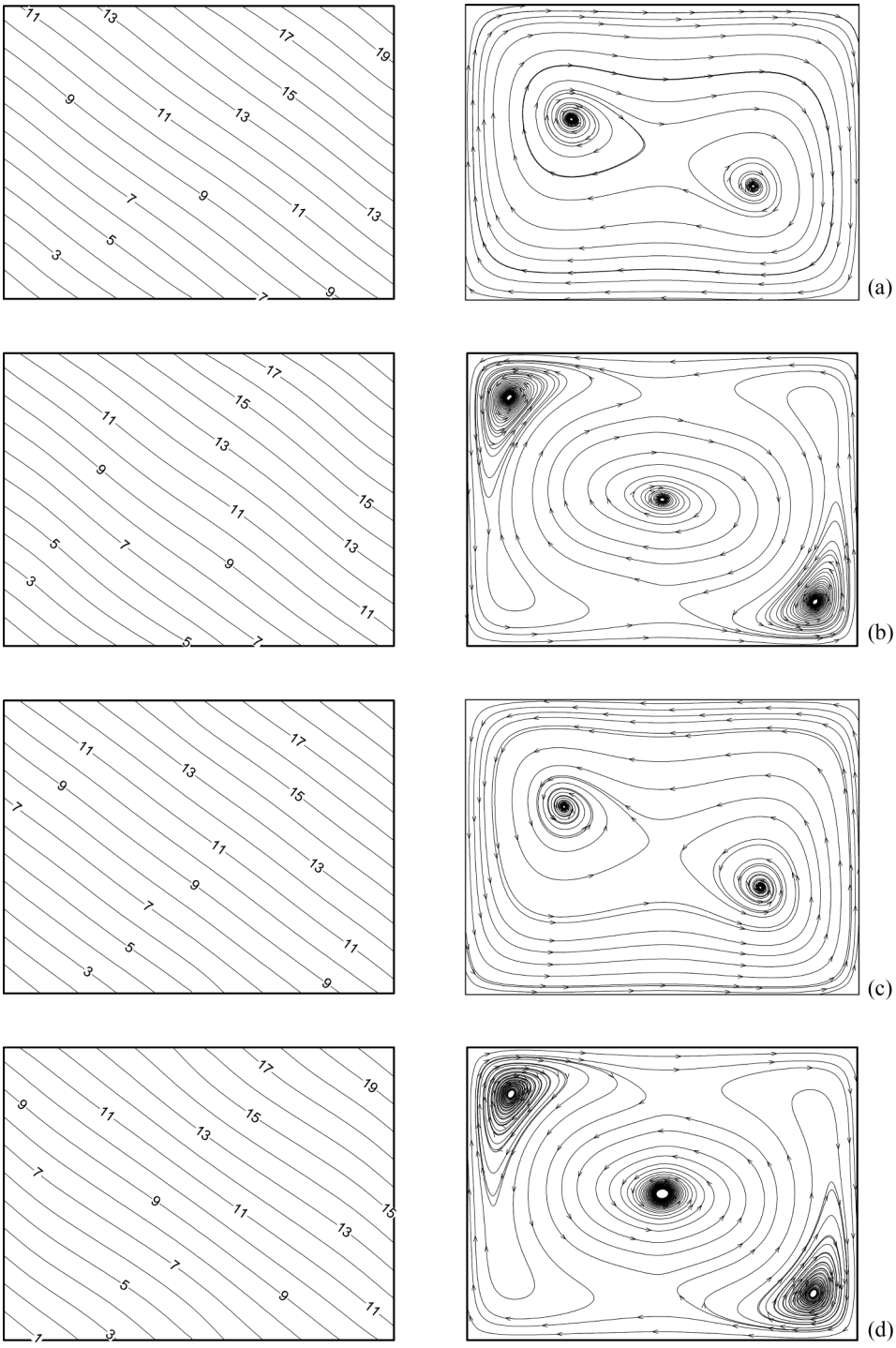

FIG. 14. Snapshots of temperature distribution (left) and velocity field (right) in the meridian plane xz ($\varphi = 0$) at four instants evenly space in time during the period τ of oscillation (case C) (contour legend: level $1 \rightarrow T = -0.45$, level $20 \rightarrow T = 0.45$, and $\Delta_{\text{level}} \rightarrow 0.05$): (a) $t = t_0$, (b) $t = t_0 + \tau/4$, (c) $t = t_0 + \tau/2$, and (d) $t = t_0 + 3\tau/4$ ($\tau = 2\pi/\varpi$).

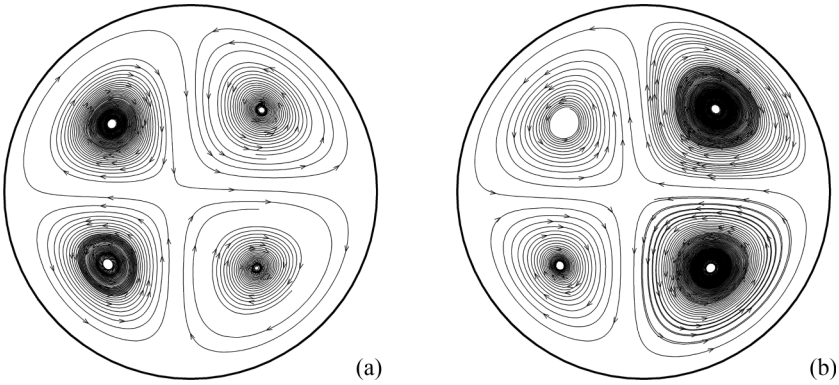

FIG. 15. Snapshots of velocity field in the cross section $z = 0$ at two instants during the period τ of oscillation (case C): (a) $t = t_0$, (b) $t = t_0 + \tau/2$ ($\tau = 2\pi/\varpi$).

C. Inclined temperature gradient

For the sake of completeness, in this section we finally discuss the case with an inclined temperature gradient, which may be regarded as a hybrid configuration bridging the gap between the two limit conditions presented in the earlier sections.

1. Thermofluid-dynamic field

Given the relatively small value of the Gershuni number, the temperature distribution is still approximately linear inside the cylindrical enclosure [it is characterized by isotherms inclined with respect to the axial direction and uniformly distributed in space (Fig. 14, left)]. The velocity field, however, displays a structure much more complex than those obtained for the other considered heating conditions. This time, clearly distinguishable convective cells can be observed in both the xz plane and sections perpendicular to the cylinder axis (four distinct vortices can be identified in Figs. 15 and 16). Like the situation considered in Sec. III A, such cells are not steady in time and change the sense of rotation periodically. A more precise idea of the three-dimensional complexity of the flow in this case can be obtained by taking a look at the snapshots of azimuthal velocity isosurfaces shown in Fig. 17.

2. Particle structures

Figure 18 illustrates that despite the increased complexity, the resulting particle accumulation structures are rather similar to those seen for the case of an axial temperature gradient. Interestingly, however, as evident in Fig. 18(a) (which shows a lateral view of the system), the extension along the axial direction of the region affected by the presence of particles (in such a figure the white area between the external system boundary and the internal darker region indicates that the zone that has been completely depleted of particles) is reduced with respect to Fig. 10. This indicates that the

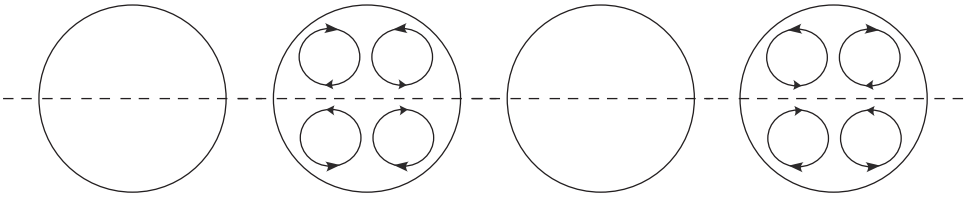

FIG. 16. Sequence (sketch) showing the evolution of vibration-induced convective cells in the generic cross section $z =$ const during one period of oscillation for case C.

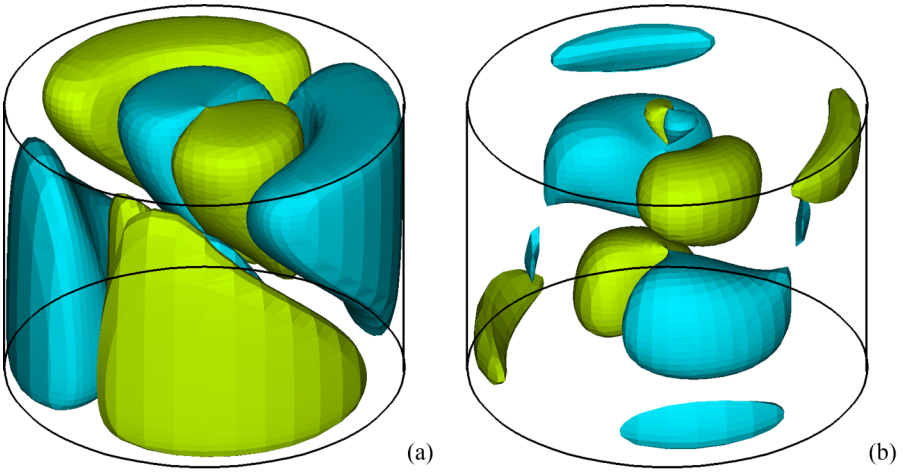

FIG. 17. Snapshots of three-dimensional isosurfaces of azimuthal velocity component w ($w = \pm 1$) for the same conditions considered in Fig. 12: (a) $t = t_0$ and (b) $t = t_0 + \tau/4$.

inclination of the imposed temperature gradient can be used to produce an axial compression of the particle pattern.

Moreover, accurate inspection of the lateral view reveals that some internal particle structures can be identified. Such structures, which were not present in Fig. 10 and look like the curved branches of a tree [Fig. 18(a)], should be ascribed to the joint action exerted on the system by the axial component of imposed vibrations and the component of the imposed temperature gradient along the x axis (via the mechanism illustrated in Sec. III B 2, which will tend to produce closed circuits like those seen in Fig. 13).

IV. DISCUSSION

As highlighted in Sec. II, hydrodynamic interactions (assumed to be absent under the assumption of a dilute solid-liquid system) play no role in the present dynamics. The cause-and-effect relationships driving particle clustering must therefore be located elsewhere.

As discussed to a certain extent in the earlier section, for the considered phenomena vibrations will be exerting their influence on particles via different separate mechanisms, one being the direct effect of the resulting accelerations on the particles due to their different density with respect to the

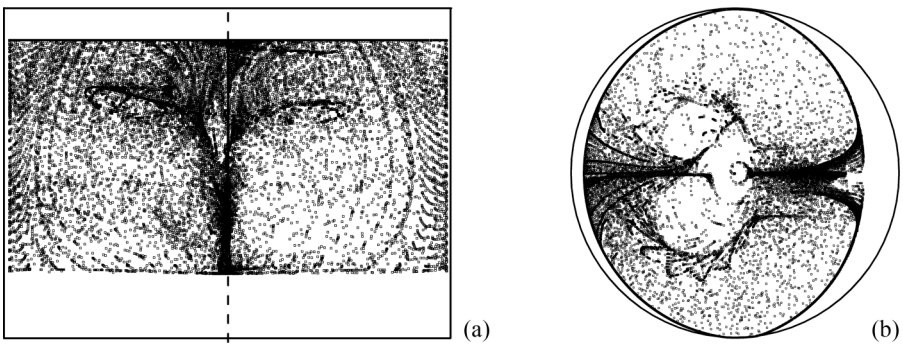

FIG. 18. Snapshot of particle aggregates [lateral and top views (case C)].

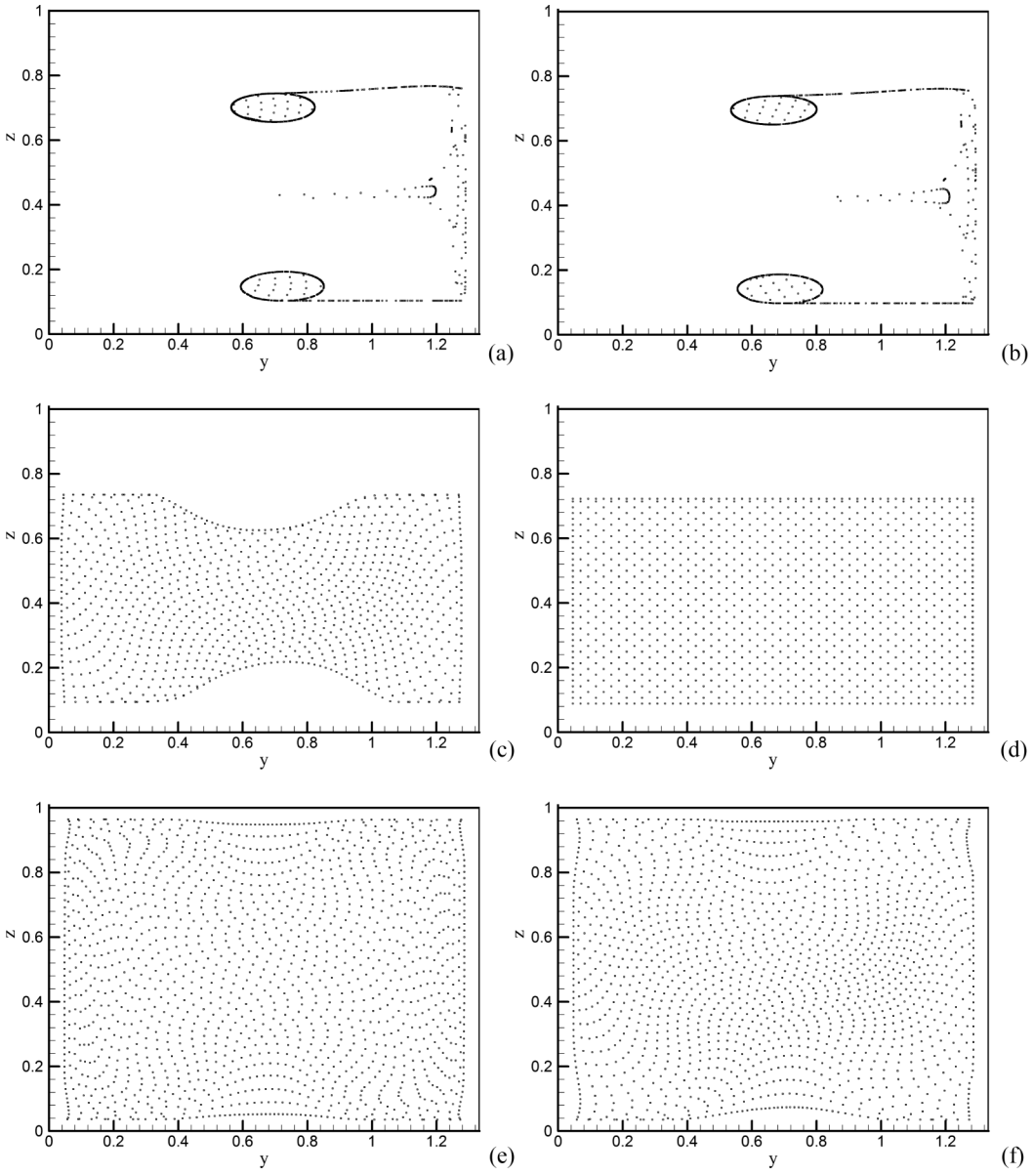

FIG. 19. Snapshot of particle aggregates (plane yz) in the case B ($t = 5.6 \times 10^{-1}$) for different conditions: (a) particles transported by the effective velocity field and subjected to the vibrational body force (full system), (b) particles transported by the velocity field obtained subtracting the mean flow from the effective velocity distribution and subjected to the vibrational body force, (c) particles transported by the mean flow only and subjected to the vibrational body force, (d) particles subjected to vibrations in an isothermal system, (e) particles transported by the mean flow only neglecting the oscillatory vibrational body force, and (f) particles transported by the effective (total) oscillatory flow neglecting the oscillatory vibrational body force.

surrounding fluid (which would still be present in an isothermal system) and the other being related to the way by which the flow of thermovibrational nature tends to transport particles according to their size and drag. The latter can be further split into a mean effect (i.e., how the time-averaged velocity field can influence the transports of particles) and an instantaneous effect related to the

periodic velocity $\mathbf{V}' = \mathbf{V} - \langle \mathbf{V} \rangle$ oscillating in time at the same acceleration frequency ω of the imposed inertial disturbance.

In order to discern clearly the contribution brought to the pattern by each of the above mechanisms, this section is finally devoted to an examination of the distinct behaviors that are produced when the influence of such effects is explored separately. This approach is generally known as modeling hierarchy and consists of a diversity of model types in which various processes are switched on and off and the results are carefully examined. More precisely, we compare the results of the computations obtained for the following different conditions: (a) particles transported by the effective velocity field and subjected to the vibrational body force (full system), (b) particles transported by the velocity field obtained subtracting the mean flow from the effective velocity distribution (particles still subjected to the vibrational body force), (c) particles transported by the mean flow only (still subjected to the vibrational body force), (d) particles subjected to the oscillatory body force in an isothermal system, (e) particles transported by the mean flow only neglecting the oscillatory body force, and (f) particles transported by the effective (total) flow neglecting the oscillatory body force.

We focus again on the same case already used for code validation, namely, the cylindrical enclosure with a nonisothermal sidewall and adiabatic ends with vibrations along the z axis, for which we could measure precisely the size of the particle structures in the yz plane (Fig. 12 and Table II). Figures 19(a) and 19(b) immediately reveal that, apart from a very small displacement towards left of the resulting particle loops in Fig. 19(b) [with respect to those in Fig. 19(a)], subtracting the mean field from the total velocity field does not change significantly the pattern (from either a quantitative or a qualitative point of view). Conversely, the lack of recognizable structures in Fig. 19(c) clearly indicates that the oscillatory component of the velocity field $\mathbf{V}' = \mathbf{V} - \langle \mathbf{V} \rangle$ is an essential ingredient without which particles do not undergo significant clustering. Indeed, although some distortion of the initially uniform distribution of particles can be seen (in agreement with the expected effect of the quadrupolar velocity field shown in Fig. 4), particles do not form dense structures. Among other things, such an argument is further supported by the results shown in Fig. 19(d), where in the complete absence of convective flow, the pattern attains a trivial configuration (the particles retain a more or less even distribution; the compression of the pattern along the vertical direction being due to the body force that periodically displays it up and down). Figures 19(e) and 19(f) finally show that when the oscillatory thermovibrational body force is neglected, neither the mean flow field nor the total field can produce particle structures (the effect of the mean velocity being limited to a weak distortion of the initial uniform particle distribution used as initial condition).

All these arguments taken together provide additional evidence of the conclusion that the coexistence of an oscillatory body force and a velocity field oscillating in time should be regarded as a necessary prerequisite for the emergence of recognizable particle agglomerates for the conditions considered here. By contrast, the role played by the time-averaged flow can be assumed to be almost negligible in terms of particle clustering phenomena.

V. CONCLUSION

Although, in a rather unexpected way, the multiplicity of the resulting recognizable accumulation structures (particle-dense surfaces) is two for all cases considered (two more or less regular tubular structures are visible in Figs. 10, 12, and 18, regardless of whether the temperature gradient is parallel, perpendicular, or inclined with respect to the symmetry axis of the cylindrical enclosure), their spatial extension (percentage of physical volume occupied) and separation (spatial distance) change significantly. As shown by the numerical results, the intriguing diversity of particle agglomerates when the direction of the imposed temperature gradient is changed (while maintaining vibrations perpendicular to it) results from the different role or importance played by (curved or straight) boundaries in constraining particles and from the different topology of the resulting (large-scale) oscillatory thermovibrational flow (whereas the time-averaged part of the flow does not provide a substantial contribution in terms of particle clustering dynamics).

In view of the generality of the mechanisms involved, we expect the importance of this category of structure-forming processes to create an opportunity for new strategies for the separation of phases in typical industrial applications involving cylindrical cavities or systems. There is a variety of fabrication processes (in which distinct components have to be fractionated) that may be considered as relevant examples of situations where the concepts elaborated in this work may have very interesting applications. Although some general (qualitative) trends about the dependence of the present phenomena on the vibration frequency and amplitude (which in the present study were fixed) may be elaborated *a priori* on the basis of earlier analyses dealing with the cubic cavity [12], future work should be devoted to parametric quantitative evaluation of the influence of the problem nondimensional parameters on the formation time and the size and position in space of the particle structures revealed here.

[1] J. Segurado, C. González, and J. LLorca, A numerical investigation of the effect of particle clustering on the mechanical properties of composites, Acta Mater. **51**, 2355 (2003).
[2] S. Hassan, T. P. Lyubimova, D. V. Lyubimov, and M. Kawaji, Effects of vibrations on particle motion near a wall: Existence of attraction force, Int. J. Multiphase Flow **32**, 1037 (2006).
[3] M. Lappa, On the nature, formation and diversity of particulate coherent structures in microgravity conditions and their relevance to materials science and problems of astrophysical interest, Geophys. Astrophys. Fluid Dyn. **110**, 348 (2016).
[4] D. Melnikov, D. Pushkin, and V. Shevtsova, Accumulation of particles in time-dependent thermocapillary flow in a liquid bridge. Modeling of experiments, Eur. Phys. J. Spec. Top. **192**, 29 (2011).
[5] D. E. Melnikov, D. O. Pushkin, and V. M. Shevtsova, Synchronization of finite-size particles by a traveling wave in a cylindrical flow, Phys Fluids **25**, 092108 (2013).
[6] I. Ueno, Y. Abe, K. Noguchi, and H. Kawamura, Dynamic particle accumulation structure (PAS) in half-zone liquid bridge—Reconstruction of particle motion by 3-D PTV, Adv. Space Res. **41**, 2145 (2008).
[7] M. Gotoda, T. Sano, T. Kaneko, and I. Ueno, Evaluation of existence region and formation time of particle accumulation structure (PAS) in half-zone liquid bridge, Eur. Phys. J. Spec. Top. **224**, 299 (2015).
[8] D. Pushkin, D. Melnikov, and V. Shevtsova, Ordering of Small Particles in One-Dimensional Coherent Structures by Time-Periodic Flows, Phys. Rev. Lett. **106**, 234501 (2011).
[9] D. Schwabe, S. Tanaka, A. Mizev, and H. Kawamura, Particle accumulation structures in time-dependent thermocapillary flow in a liquid bridge under microgravity, Microgravity Sci. Technol. **18**, 117 (2006).
[10] D. Schwabe and A. I. Mizev, Particles of different density in thermocapillary liquid bridges under the action of travelling and standing hydrothermal waves, Eur. Phys. J. Spec. Top. **192**, 13 (2011).
[11] V. G. Kozlov, A. A. Ivanova, and P. Evesque, Block stratification of sedimenting granular matter in a vessel due to vertical vibration, Fluid Dyn. Mater. Process. **2**, 203 (2006).
[12] M. Lappa, The patterning behaviour and accumulation of spherical particles in a vibrated non-isothermal liquid, Phys. Fluids **26**, 093301 (2014).
[13] E. Crespo del Arco and P. Bontoux, Numerical simulations and analysis of axisymmetric convection in a vertical cylinder: An effect of Prandtl number, Phys. Fluids A **1**, 1348 (1989).
[14] E. Crespo del Arco, P. Bountoux, R. L. Sani, G. Hardin, and G. P. Extrémet, Steady and oscillatory convection in vertical cylinders heated from below. Numerical simulation of asymmetric flow regimes, Adv. Space Res. **8**, 281 (1988).
[15] C. Smutek, P. Bontoux, B. Roux, G. H. Schiroky, and A. C. Hurford, Three-dimensional convection in horizontal cylinders—Numerical solutions and comparison with experimental and analytical results, Numer. Heat Transfer A: Appl. **8**, 613 (1985).
[16] P. Bontoux, B. Roux, G. H. Schiroky, B. L. Markham, and F. Rosenberger, Convection in the vertical midplane of a horizontal cylinder. Comparison of two-dimensional approximations with three-dimensional results, Int. J. Heat Mass Transfer **29**, 227 (1986).

[17] P. Bontoux, C. Smutek, B. Roux, and J. M. Lacroix, Three-dimensional buoyancy-driven flows in cylindrical cavities with differentially heated endwalls. Part 1. Horizontal cylinders, J. Fluid Mech. **169**, 211 (1986).
[18] S. Vaux, H. Ben Hadid, and D. Henry, Study of the hydrodynamic instabilities in a differentially heated horizontal circular cylinder corresponding to a Bridgman growth configuration, J. Cryst. Growth **290**, 674 (2006).
[19] I. H. Brooks and S. Ostrach, An experimental investigation of natural convection in a horizontal cylinder, J. Fluid Mech. **44**, 545 (1970).
[20] S. Ostrach and R. G. Hantman, Natural convection inside a horizontal cylinder, Chem. Eng. Commun. **9**, 213 (1981).
[21] S. Xin, P. Le Quéré, and O. Daube, Natural convection in a differentially heated horizontal cylinder: Effects of Prandtl number on flow structure and instability, Phys. Fluids **9**, 1014 (1997).
[22] A. Y. Gelfgat, P. Z. Bar-Yoseph, and A. Solan, Axisymmetry breaking instabilities of natural convection in a vertical Bridgman growth configuration, J. Cryst. Growth **220**, 316 (2000).
[23] J. I. D. Alexander, J. Ouazzani, and F. Rosenberger, Analysis of the low gravity tolerance of Bridgman-Stockbarger crystal growth, II. Transient and periodic accelerations, J. Cryst. Growth **113**, 21 (1991).
[24] J. I. D. Alexander, J.-P. Garandet, J. J. Favier, and A. Lizee, g-jitter effects on segregation during directional solidification of tin-bismuth in the MEPHISTO furnace facility, J. Cryst. Growth **178**, 657 (1997).
[25] M. Wadih and B. Roux, Natural convection in a long vertical cylinder under gravity modulation, J. Fluid Mech. **193**, 391 (1988).
[26] E. V. Zharikov, L. V. Prihodko, and N. R. Storozhev, Fluid flow formation resulting from forced vibration of a growing crystal, J. Cryst. Growth **99**, 910 (1990).
[27] A. A. Wheeler, G. B. McFadden, B. T. Murray, and S. R. Coriell, Convective stability in the Rayleigh-Bénard and directional solidification problems: high-frequency gravity modulation, Phys. Fluids A **3**, 2847 (1991).
[28] B. T. Murray, S. R. Coriell, and G. B. McFadden, Proceedings of the VIIIth European Symposium on Materials and Fluid Sciences in Microgravity, Brussels, 1992 (unpublished).
[29] B. T. Murray, S. R. Coriell, G. B. McFadden, A. A. Wheeler, and B. V. Saunders, Gravitational modulation of thermosolutal convection during directional solidification, J. Cryst. Growth **129**, 70 (1993).
[30] A. A. Ivanova and V. G. Kozlov, Thermal vibrational convection in a cavity under nontranslational oscillations, Fluid Dyn. **38**, 372 (2003).
[31] V. G. Kozlov and N. V. Selin, Pendulum thermal vibrational convection in a liquid layer with internal heat generation, Fluid Dyn. Mater. Process. **2**, 107 (2006).
[32] H. C. Kuhlmann, M. Lappa, D. Melnikov, R. Mukin, F. H. Muldoon, D. Pushkin, V. S. Shevtsova, and I. Ueno, The JEREMI-project on thermocapillary convection in liquid bridges. Part A: Overview of particle accumulation structures, Fluid Dyn. Mater. Process. **10**, 1 (2014).
[33] M. Lappa, Assessment of the role of axial vorticity in the formation of particle accumulation structures in supercritical Marangoni and hybrid thermocapillary-rotation-driven flows, Phys. Fluids **25**, 012101 (2013).
[34] M. Lappa, Stationary solid particle attractors in standing waves, Phys. Fluids **26**, 013305 (2014).
[35] M. Lappa, On the existence and multiplicity of one-dimensional solid particle attractors in time-dependent Rayleigh-Bénard convection, Chaos **23**, 013105 (2013).
[36] R. Monti, R. Savino, and M. Lappa, On the convective disturbances induced by g-jitter on the space station, Acta Astronaut. **48**, 603 (2001).
[37] M. Lappa and L. Carotenuto, Effect of convective disturbances induced by g-jitter on the periodic precipitation of lysozyme, Microgravity Sci. Tech. **14**, 41 (2003).
[38] R. Savino and M. Lappa, Assessment of the thermovibrational theory: Application to g-jitter on the space-station, J. Spacecraft Rockets **40**, 201 (2003).
[39] A. Mialdun, I. I. Ryzhkov, D. E. Melnikov, and V. Shevtsova, Experimental Evidence of Thermal Vibrational Convection in a Nonuniformly Heated Fluid in a Reduced Gravity Environment, Phys. Rev. Lett. **101**, 084501 (2008).

[40] V. Shevtsova, A. Mialdun, D. Melnikov, I. Ryzhkov, Y. Gaponenko, Z. Saghir, T. Lyubimova, and J. C. Legros, The IVIDIL experiment onboard the ISS: Thermodiffusion in the presence of controlled vibrations, C. R. Mec. **339**, 310 (2011).

[41] M. Lappa, On the variety of particle accumulation structures under the effect of g-jitters, J. Fluid Mech. **726**, 160 (2013).

[42] M. Lappa, Control of convection patterning and intensity in shallow cavities by harmonic vibrations, Microgravity Sci. Technol. **28**, 29 (2016).

[43] M. R. Maxey and J. J. Riley, Equation of motion for a small rigid sphere in a nonuniform flow, Phys. Fluids **26**, 883 (1983).

[44] F. Balboa Usabiaga, I. Pagonabarraga, and R. Delgado-Buscalioni, Inertial coupling for point particle fluctuating hydrodynamics, J. Comput. Phys. **235**, 701 (2013).

[45] A. Esmaeeli, Phase distribution of bubbly flows under terrestrial and microgravity conditions, Fluid Dyn. Mater. Process. **1**, 63 (2005).

[46] J. J. Derksen and D. Eskin, Flow-induced forces in agglomerates, Fluid Dyn. Mater. Process. **7**, 341 (2011).

[47] D. Langbein, Motion of ensembles of spherical particles in a fluid due to g-jitter, Adv. Space Res. **11**, 189 (1991).

[48] S. Hassan and M. Kawaji, The effects of vibrations on particle motion in a viscous fluid cell, J. Appl. Mech. **75**, 031012 (2008).

[49] C. A. J. Fletcher, *Computational Techniques for Fluid-Dynamics* (Springer, Berlin, 1991).

[50] H. Khallouf, G. Z. Gershuni, and A. Mojtabi, Numerical study of two-dimensional thermo-vibrational convection in rectangular cavities, Numer. Heat Transfer A **27**, 297 (1995).